JGR Space Physics

RESEARCH ARTICLE
10.1029/2021JA029869

Constraining the Upper Level Vibrational Populations of the N_2 Lyman-Birge-Hopfield Band System Using GOLD Mission's Dayglow Observations

Saurav Aryal[1], J. Scott Evans[2], J. M. Ajello[1,3], S. C. Solomon[4], A. W. Burns[4], R. W. Eastes[1], and W. E. McClintock[1]

[1]Laboratory for Atmospheric and Space Physics, University of Colorado Boulder, Boulder, CO, USA, [2]Computational Physics Inc, Springfield, VA, USA, [3]Jet Propulsion Laboratory, California Institute of Technology, Pasadena, CA, USA, [4]High Altitude Observatory, National Center for Atmospheric Research, Boulder, CO, USA

Key Points:

- N_2 Lyman-Birge-Hopfield (LBH) band vibrational populations are quantified using Global-scale Observations of Limb and Disk mission's disk and limb dayglow observations
- Variations in LBH vibrational populations due to solar zenith angle and tangent altitude are insignificant
- Disk temperature retrievals based on LBH emissions can use same set of vibrational populations

Correspondence to:
S. Aryal,
saurav.aryal@lasp.colorado.edu

Citation:
Aryal, S., Evans, J. S., Ajello, J. M., Solomon, S. C., Burns, A. W., Eastes, R. W., & McClintock, W. E. (2022). Constraining the upper level vibrational populations of the N_2 Lyman-Birge-Hopfield band system using GOLD mission's dayglow observations. *Journal of Geophysical Research: Space Physics*, *127*, e2021JA029869. https://doi.org/10.1029/2021JA029869

Received 9 AUG 2021
Accepted 4 SEP 2022
Corrected 27 OCT 2022

This article was corrected on 27 OCT 2022. See the end of the full text for details.

Author Contributions:
Conceptualization: J. M. Ajello, S. C. Solomon, R. W. Eastes, W. E. McClintock
Formal analysis: Saurav Aryal
Funding acquisition: R. W. Eastes
Investigation: R. W. Eastes
Methodology: Saurav Aryal, J. Scott Evans, J. M. Ajello, R. W. Eastes, W. E. McClintock
Project Administration: R. W. Eastes
Software: Saurav Aryal, J. Scott Evans, S. C. Solomon, W. E. McClintock

Abstract Current and previous thermospheric remote sensing missions use N_2 Lyman-Birge-Hopfield (LBH) band dayglow emission measurements to retrieve line-of-sight thermospheric composition and temperature. The precision of thermospheric composition and temperature retrieved from observations depends on the uncertainty in the relative LBH vibrational populations. In the laboratory, electron impact induced LBH emission measurements have shown that the relative vibrational populations change with gas pressure. However, it is not fully understood how these populations change for dayglow observations where the emissions that contribute to the observations vary with solar illumination and line-of-sight geometry. We quantify the relative vibrational populations as a function of solar zenith angle (SZA) and tangent altitude using Global-scale Observations of Limb and Disk mission's LBH dayglow observations. We find that, while some lower vibrational levels show potential enhancement with increasing pressure (decreasing altitude), in general, they do not change significantly with SZA or tangent altitude for dayglow observations. The vibrational populations can thus be assumed as fixed parameters when retrieving neutral disk temperatures from remotely sensed LBH dayglow observations.

1. Introduction

Emissions from the N_2 Lyman-Birge-Hopfield (LBH) band system ($a^1\Pi_g \rightarrow X^1\Sigma_g^+$) have been used extensively for thermospheric remote sensing (e.g., Budzien et al., 1994; Eastes et al., 1985, 2017; Evans et al., 2020; Paxton et al., 1999). Neutral disk thermospheric temperatures can be retrieved from the rotational structure of LBH bands. Temperature retrievals are typically performed utilizing data-model comparisons, either using look-up tables or least-squares fitting (e.g., Aksnes et al., 2006; Meier et al., 2015, etc.). Similarly, thermospheric compositions can be derived from LBH (and OI 135.6 nm) brightnesses. Therefore, the reliability of derived thermospheric temperature and composition depend on accurate LBH emission models. However, discrepancies between observations and simulations have been reported (e.g., Budzien et al., 1994). Such discrepancies indicate that LBH vibrational populations based solely on theoretical Frank-Condon factors (FCF) do not adequately represent the observed LBH band excitation mechanisms.

LBH band emissions arise from cascade and direct excitation. The cascade processes are mediated by transition to and from two nearby states: $a'^1\Sigma_g^- \leftrightarrow a^1\Pi_g$ and $w^1\Delta_u \leftrightarrow a^1\Pi_g$. Cascade excitation occurs via two mechanisms: radiative transitions and collision induced electronic transitions (CIET). The CIET mechanism (please see Eastes & Dentamaro, 1996, and references therein for details) is pressure dependant, and in the Earth's atmosphere will vary with altitude. The $a^1\Pi_g$ (referred as a-state hereafter) state's vibrational population distributions (v') and their total sum (the emission cross section) provide information on LBH emission processes. Here we provide a brief overview of the historical context of LBH cross section and vibrational population measurements and estimates of cascade contributions. For a more detailed history, see Ajello et al. (2010).

Early laboratory measurement of electron impact induced LBH emission by Ajello (1970) saw that lower vibrational populations ($v' < 2$) increased with pressure. This was attributed to collisional transfer of vibrational energy from upper to lower v' levels at higher pressures. A follow up measurement by Ajello and Shemansky (1985) found that the cascade contribution to LBH emission was small (<5%) and only the lower v' populations deviated from theory at energies <20 eV. This deviation at lower energies was attributed to energy threshold effects

Supervision: J. Scott Evans, J. M. Ajello, A. W. Burns, R. W. Eastes, W. E. McClintock
Validation: Saurav Aryal, J. Scott Evans, R. W. Eastes
Writing – original draft: Saurav Aryal
Writing – review & editing: Saurav Aryal, J. Scott Evans, R. W. Eastes

(lower levels get excited at smaller energies). The LBH cross section were measured by Cartwright, Chutjian, et al. (1977); Cartwright, Trajmar, et al. (1977) and modeled (along with relative vibrational populations) in auroras by Cartwright (1978). Their cross section estimation agreed well with measurements by Ajello and Shemansky (1985) where the cascade contribution was minor. These early studies suggested either that the cascade contribution to LBH emissions are negligible or that the measurement predominantly captured direct emission. A limiting factor for early lab measurements had been the size of the electron-impact chamber. While LBH emissions from direct excitation can only occur up to 10 cm from the impact center, the cascade emissions with their longer lifetime occur more easily beyond the 10 cm limit (Ajello et al., 2017). Ajello and Shemansky (1985) used a chamber (32 cm in diameter) that they estimated covered 72% of the radiation field. Recent laboratory measurements performed inside a large chamber (~1.2 m in diameter) have isolated the cascade contribution to LBH emission (Ajello et al., 2017, 2020). It was seen that the $v' < 2$ populations were always enhanced for cascade emissions and this enhancement increased with gas pressure. Earth's N_2 LBH dayglow emission occurs via photo-electron impact at different pressures (altitudes). However, variability in the LBH emission cross section and vibrational populations for daytime observations has not been adequately quantified. Thus, laboratory measurement of electron-impact induced LBH v' populations and the emission cross sections by Ajello and Shemansky (1985) or Young et al. (2010) have been used by most researchers.

Early analyses of the relative LBH vibrational populations using dayglow measurements were reported by Eastes et al. (1985) and Budzien et al. (1994). Budzien et al. (1994) showed that the LBH cascade emission contribution was more significant (45% of direct emission) than expected. Consequently, the observed LBH brightnesses were about 1.4–1.6 times higher than model calculations that excluded cascade effects. Other studies have used different scale factors to account for cascade effects in modeling LBH dayglow brightness (e.g., Strickland et al., 2004, use a scale factor of 1.4). Eastes (2000) attempted to calculate cascade effects when modeling the LBH emissions. Their modeled brightness was 1.55 times brighter when cascade effects (both radiative + CIET) were included. This factor (1.55) is consistent with the factor used by Budzien et al. (1994) (1.4–1.6) to match their model with dayglow observations. However, Eastes (2000) used significant assumptions in their analysis.

The Global-scale Observations of Limb and Disk (GOLD, Eastes et al., 2017) spectrograph onboard the SES-14 commercial satellite has been making LBH dayglow measurement since late 2018 from a geo-stationary orbit. GOLD's synoptic thermospheric LBH observations have already contributed to new understanding of eclipse induced composition (Aryal et al., 2020) and geomagnetic storm induced temperature (Laskar et al., 2021) changes. GOLD's high resolution (~0.2 nm), high signal-to-noise (SNR) dayglow measurements allow better separation of LBH bands. Better separation of the bands result in reduced degeneracy between the vibrational populations and the rotational temperature during retrievals. Thus, GOLD observations improve the quantification of the LBH vibrational populations and rotational temperatures compared to previous missions. Using GOLD's limb observations, vibrational populations at tangent altitudes of 100–150, 150–200, and 200–250 km were recently reported (Figure 4 in Ajello et al., 2020). Enhancements were seen in the lower vibrational levels ($v' < 2$), especially at 100–150 km where the atmospheric pressure is higher than 150–200 and 200–250 km. Laboratory derived vibrational populations from the paper also show enhanced low v' populations at pressures (~5 mTorr) comparable to the lower thermosphere (Figure 8 in Ajello et al., 2020). While these enhancements have mostly been attributed to cascade effects, energy threshold effects also have a minor contribution. In this paper, we expand on the observationally constrained analysis of Ajello et al. (2020) by quantifying variations in dayglow LBH vibrational populations as a function of altitude (i.e., pressure) for different seasons and geographic locations. We also quantify the dayglow LBH vibrational populations at different solar zenith angles (SZA) using GOLD's disk measurements. The primary objective of this study is to determine if relative LBH vibrational populations vary significantly with SZA or tangent altitudes for dayglow observations. This will enable better modeling of thermospheric LBH dayglow observations using GOLD or other FUV missions.

2. Observation Data

GOLD is an FUV imaging spectrometer (~133–165 nm) and sits above 47°W longitude in a geo-stationary orbit. GOLD's three interchangeable entrance slits can be selected to achieve different resolutions (0.21, 0.35, or 2.16 nm). GOLD's two identical channels, each with its own mirror, can independently scan the Earth's upper atmosphere. Eastes et al. (2017), McClintock, Eastes, Hoskins, et al. (2020), and McClintock, Eastes, Beland, et al. (2020) provide more details on the GOLD instrument and its operations. Since its launch in late 2018,

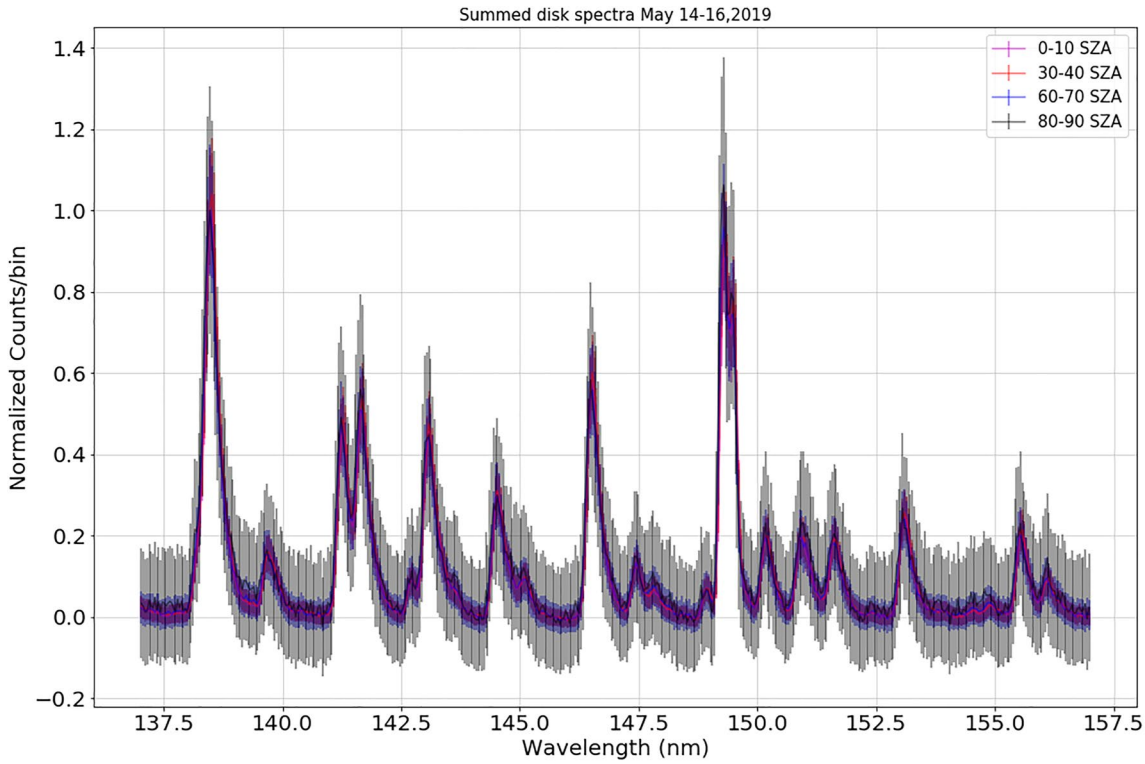

Figure 1. Normalized (to 138.3 nm peak) Global-scale Observations of Limb and Disk (GOLD) mission's disk spectra (137–155 nm) from 14–16 May 2019. Observations are from 5 to 10°N geographic latitude and 40–50° longitude. They are further binned by solar zenith angle (SZA): 0–10° (magenta), 30–40° (red), 60–70° (blue) and 80–90° (black). Measurement uncertainties (multiplied by a factor of 10) are also shown.

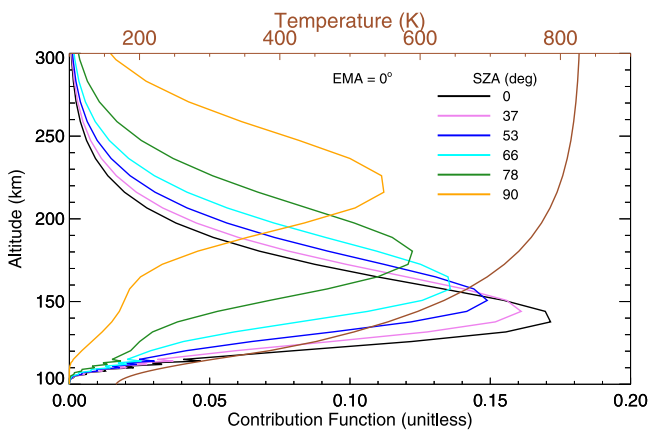

Figure 2. Altitude profiles of Lyman-Birge-Hopfield (LBH) band emission's contribution function (nadir viewing) at 0°, 37°, 53°, 66°, 78°, and 90° solar zenith angles (SZAs). Neutral temperature profile from NRLMSIS-00 model is also shown for reference (top abscissa). The contribution functions was calculated using the Atmospheric Ultraviolet Radiance Integrated Code (AURIC, Strickland et al., 2004) dayglow model in combination with the LBH band model of Budzien et al. (1994) using an NRLMSISE-00 atmosphere and NRLEUV solar irradiance spectrum (Lean et al., 2003) appropriate for solar minimum conditions. Notice that the altitude of peak contribution and the neutral temperature are both increasing with SZA. EMA = Emission Angle.

GOLD is making regular daytime disk, limb, occultation, and nighttime partial-disk scans at a cadences of 24, 6, and 15 min, respectively.

The disk dayglow scans are made by scanning from the eastern to the western limb. Northern and southern hemispheric scans are made separately (12 min cadence each) at a spectral dispersion of 0.04 nm/pixel. The disk scan's spatial resolution (in Level 1C files) is 125 km by 125 km at nadir. GOLD limb dayglow observations are made at the eastern (~34°E tangent longitude) and the western (~129°W tangent longitude) limbs in between the northern and southern hemisphere disk scans. The limb data are sampled at increments of ~16 km tangent altitude (1.25° angular). For this study, we use GOLD's disk and limb spectra (137–155 nm) observed within 5–10°N latitude and 40–50°W longitude.

Normalized spectra from GOLD's disk observations within 5–15°N geographic latitudes and 40–50°W longitude on May 14–16 2019 at 0–10°, 30–40°, 60–70°, and 80–90° SZA bins are shown in Figure 1. Since the altitude of peak LBH emission increases as the SZA increases (see Figure 2) the corresponding atmospheric pressure (altitude) is decreasing (increasing). The disk scan's spatial resolution is lower (compared to 125 km by 125 km at nadir) at higher latitude and emission angles leading to spatial smearing. We limit this smearing by only selecting data within 5°–15°N latitude and 40°–50°W longitude. We fit an LBH spectral model to each binned spectrum, allowing the vibrational populations to vary during the fit.

GOLD makes limb observations up to 450 km tangent altitude, but the data below 100 km and above 250 km have relatively poor SNR, thus, we only use

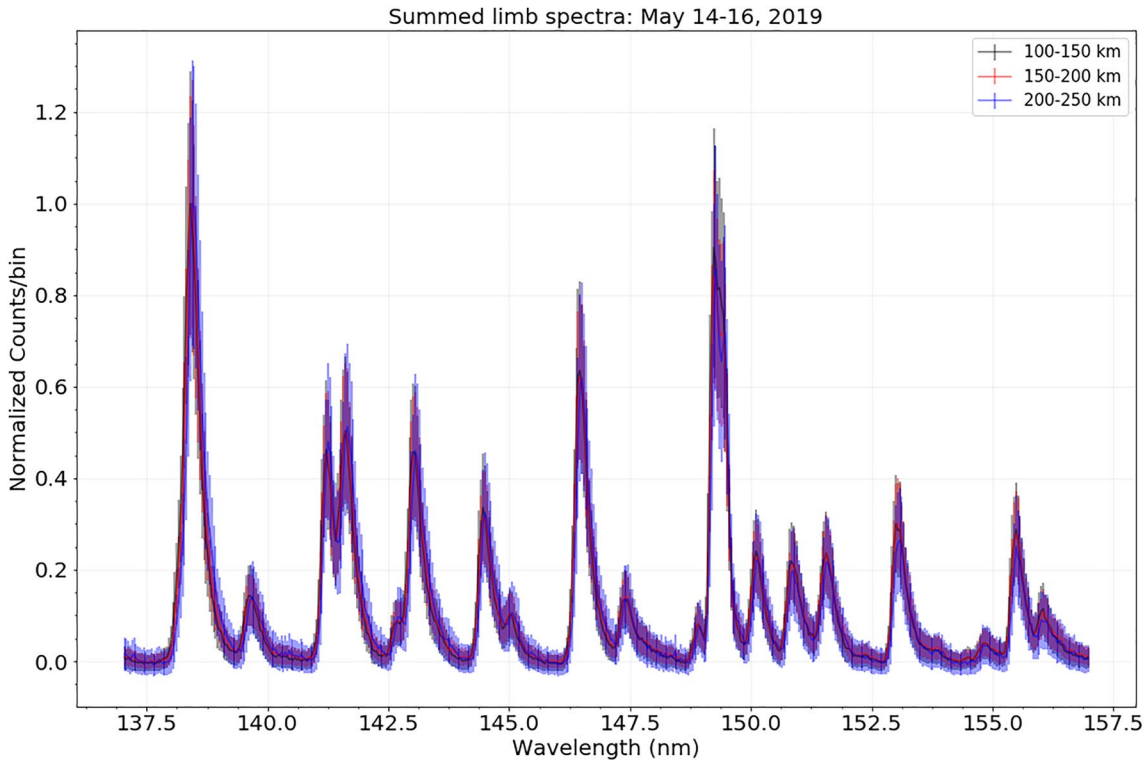

Figure 3. Normalized (to 138.3 nm peak) Global-scale Observations of Limb and Disk (GOLD) mission's limb spectra (137–157 nm) from 18 to 22 UT on 14–16 May 2019. The spectra are constrained to SZA <40° and summed from 100 to 150 km (black), 150–200 km (red) and 200–250 km (blue) tangent heights. Measurement uncertainties multiplied by a factor of 10 are also shown for each spectrum.

spectra within 100–250 km tangent altitude. Normalized limb spectra at 100–150, 150–200, and 200–250 km tangent altitudes, summed from 18 to 22 UT (western limb scans) on 14–16 May 2019 with SZA < 40° are shown in Figure 3. During a typical limb scan, a range of tangent altitudes is sampled along the slit length. This introduces smearing in the altitude dimension (especially away from the equator) when the slit gets projected onto tangent altitude grids (see Figure 1 in Evans et al., 2020). Thus, we constrain data selection to within 5°–15°N geographic latitude to limit the effect of this smearing.

3. Spectral Fitting

We use the Levenberg-Marquardt (LM, Levenberg, 1944; Marquardt, 1963) least-squares (χ^2) minimization technique to fit model spectra to GOLD's observations. We use definition of Bevington et al. (1993, Chapter 8), where χ^2 is the root square sum of the data-model residual divided by the measurement uncertainty. Here, data (spectra) is the coadded corrected counts (after flat field correction and background removal, see McClintock, Eastes, Beland, et al., 2020, for details). The spectral random uncertainty is the square root of the summed raw counts from the selected measurements. We use 15% of corrected counts as background uncertainty as suggested in GOLD's release notes (http://gold.cs.ucf.edu/wp-content/documentation/GOLD_Release_Notes_Rev4.4.pdf) and assume no sensitivity change for a given wavelength. The random and the background uncertainties are added in quadrature to estimate the total uncertainty of the coadded spectra. The LBH band model of Budzien et al. (1994) is used to generate high-resolution spectra for each of the LBH $v' = 0$–6 progressions using the FCF vibrational distribution expected for direct excitation (Benesch et al., 1966). The simulated ro-vibrational lines are shifted and convolved with a Gaussian point spread function (PSF, full width half max: ~0.01 nm) and then re-sampled match GOLD's spectral resolution (full width half max: ~0.19 nm). The Gaussian lineshape was sufficient to model pre-flight OI 135.6 nm doublet laboratory spectra measured by GOLD (McClintock, Eastes, Hoskins, et al., 2020). Contributions from atomic nitrogen multiplets at 141.2 and 149.3 nm are excluded from the fitting. The (4,2) and (3,3) LBH bands, which overlap with the 141.2 and 149.3 nm multiplets, respectively, are also excluded.

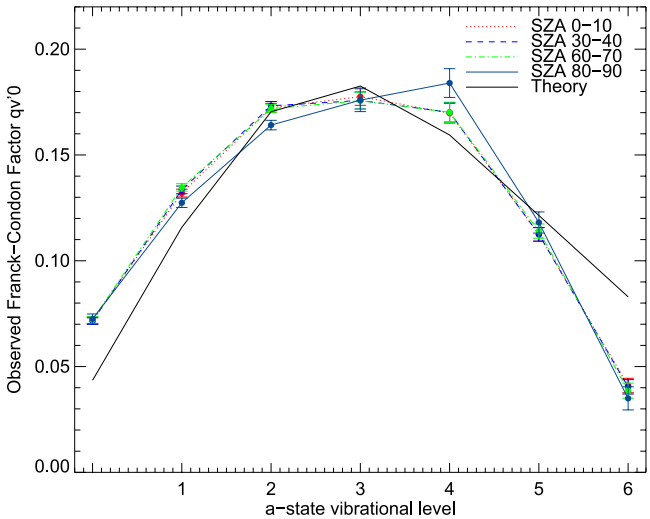

Figure 4. Derived relative vibrational populations at 0–10° (red and dotted), 30–40° (blue and dashed), 60–70° (green and dash dot) and 80–90° (cyan) solar zenith angle (SZA) bins. Relative Frank-Condon factors (FCF) vibrational populations are shown in black for reference. The spectra used to derive these populations are shown in Figure 1.

The MPFITFUN (https://www.l3harrisgeospatial.com/docs/mpfitfun.html) subroutine for the Interactive Data Language (IDL,https://www.l3harris-geospatial.com/Software-Technology/IDL) is used to perform the minimizations. Rotational temperatures are derived first, using only the (2,0) band (~137–139 nm) and FCF (from Lofthus & Krupenie, 1977) vibrational populations (as fixed parameters). The vibrational populations for $v' = 0$–6 are then derived performing the LM fit a second time using the temperature derived in the first step as a fixed parameter. Using the second step reduces the number of fit-parameters while deriving the relative vibrational populations. The 1-σ uncertainties in the retrieved temperatures and vibrational populations are obtained and scaled (by a factor of $\sqrt{\text{reduced } \chi^2}$) as described in Bevington et al. (1993, Chapter 8). The fitted vibrational populations are passed as inputs again to the band model to obtain the full LBH (110–360 nm) and individual vibrational level's brightnesses. The relative populations are then the brightness ratio of a particular vibrational level to the full LBH band. This final step accounts for the effect of pre-dissociation included in the band model (details in Section 4.1). The uncertainties of the final relative populations are assumed to be the same as the LM-fitted relative populations.

4. Results

4.1. Vibrational Populations Binned by SZA Using Disk Observations

Figure 4 shows the derived vibrational populations at 0–10°, 30–40°, 60–70°, and 80–90° SZA bins using GOLD's disk observations. The model fit to the 0–10° disk SZA spectra is shown in Figure 5 as an example. As pre-dissociation of the a-state above $v' = 6$ accounts for ~12.23% (Ajello & Shemansky, 1985) of the total FCF, all relative populations are normalized to a system total of 0.877 (appropriate for ~300 K). Following Budzien et al. (1994), for $v' = 6$ we assume 0% predissociation for rotational levels ($J' \leq 13$ and 100% for $J' > 13$. Using the temperature dependence of predissociation determined from the Budzien et al. (1994) model, we find that the error introduced by assuming a fixed total system normalization of 0.877 is ~1% for temperatures between 600 and 900 K.

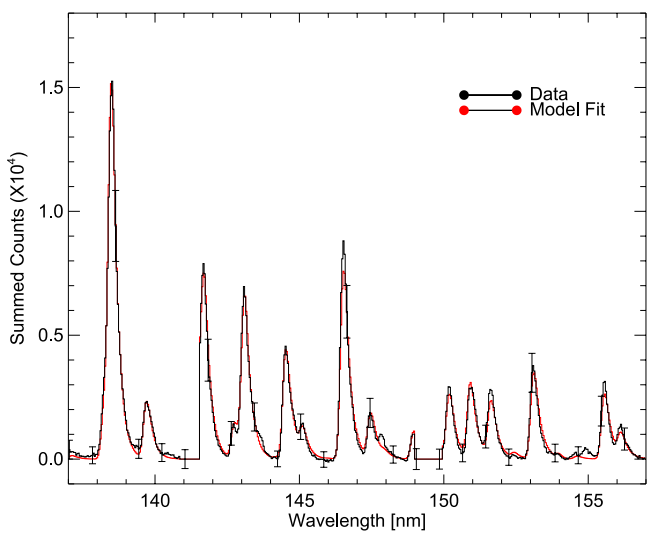

Figure 5. Comparison between the 0–10° solar zenith angle (SZA) spectra (black) and its modeled LM fit (red). Data uncertainties (times 10) are also shown at every 20 points for reference. The modeled spectra was obtained at a temperature of 621 K by optimizing the Lyman-Birge-Hopfield (LBH) band's relative vibrational populations using a LM fit.

It is seen that the relative vibrational populations at different SZA bins are quite similar. All low v′ levels (<2) are enhanced relative to the theoretical estimates. The $v' = 4$ populations are more scattered and have higher uncertainties. This most likely occurs because one of the $v' = 4$ band overlaps with the atomic 141.2 nm line and is removed from fitting, and the other $v' = 4$ bands are weaker (see Figure 6). For the 30–40° SZA case, the higher $v' = 4$ population (compared to other SZA) seems to have lowered the relative $v' = 1$ and $v' = 2$ populations due to normalization. The $v' = 6$ level populations are significantly lower (>50%) than theoretical population due to pre-dissociation. The vibrational populations at 0–10°, 30–40°, 60–70°, and 80–90° SZA are quantified in Table 1. Any minor differences in the SZA binned populations are almost negligible.

In Table 2 we examine the changes in the retrieved temperatures for three different sets of vibrational populations. The disk temperatures are retrieved for the 14–16 May 2019 SZA binned spectra using following fixed populations: (a) v' from 80 to 90° SZA and fitting 137–148 nm LBH spectra, (b) v' from 0 to 10° SZA and fitting 137–148 nm LBH spectra and (c) fitting only the (2,0) band peak with fixed FCF vibrational populations. Note that all of the temperatures are increasing with SZA as expected. While the SZA also varies with the local time (LT) and a recent study saw ~50 K change on average from 12 to 14 LT (Laskar et al., 2021), our measurements are confined to a narrow range of longitude (within 15° of nadir) and have the

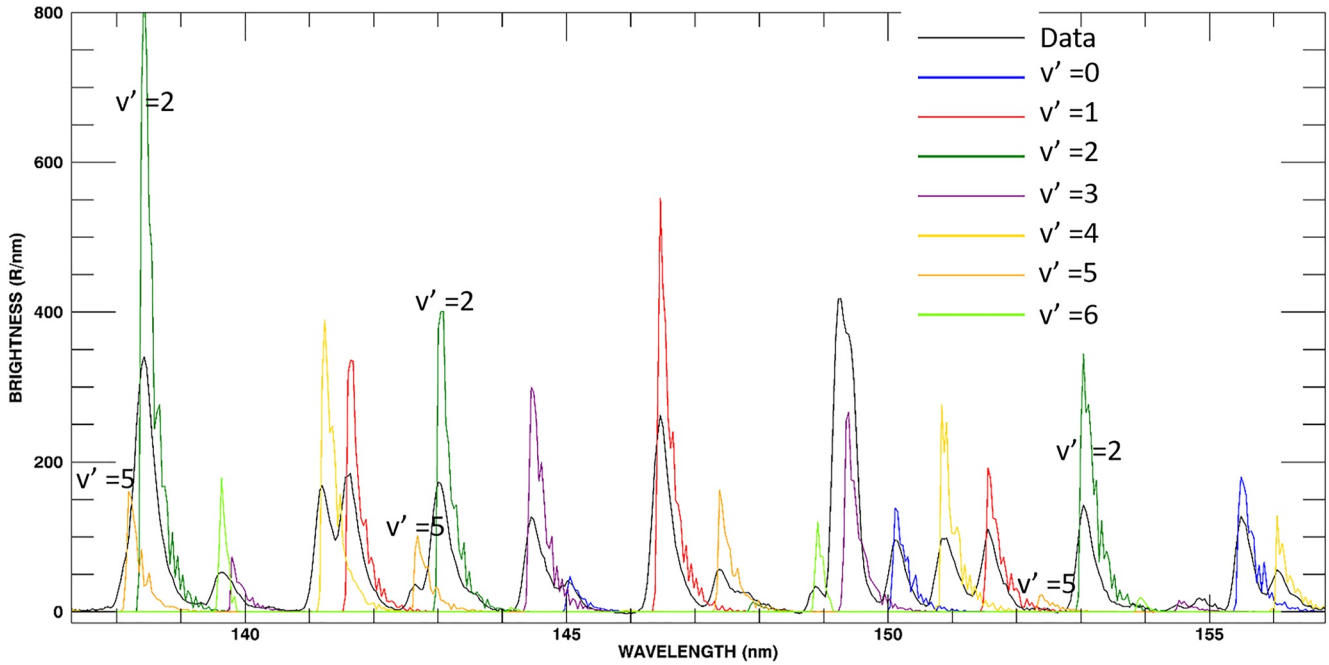

Figure 6. Summed Global-scale Observations of Limb and Disk's (GOLD's) spectra (black) and modeled spectra showing emissions from different bands (various colors). Also note a slight shift in location between model and data peaks. During fitting, a constant shift parameter accounts for the data-model mismatch in peak locations.

same average LT. The temperature increases rapidly with increasing altitude (and hence with SZA, see Figure 2) when compared to LT changes and will dominate. Disk temperatures derived using fixed vibrational populations from different SZA bins do not deviate significantly (<5 K, see Table 2). However, temperatures derived using only the (2,0) band are slightly different (~±30–50 K). This implies that any one of the SZA-binned vibrational population set could be used as fixed parameters without affecting the LBH based disk temperature retrievals.

4.2. Vibrational Populations Binned by Tangent Altitude Using Limb Observations

Figure 7 shows the derived vibrational populations for 100–150, 150–200, and 200–250 km, respectively. Averages of spectra (at SZAs <40°) from 6 to 10 UT on 14–16 May 2019 (shown in Figure 3) were fitted with the LBH spectral band model using the method described in Section 3. All the derived relative populations are normalized to 0.877. The $v' = 0$ populations are slightly enhanced for 100–150 km and 150–200 km where

Table 1
The Relative Vibrational Populations at 0–10°, 30–40°, 60–70° and 80–90° SZA Bins for 14–16 May 2019 From 14 to 16 UT

	SZA bins				
v' level	FCF	0–10°	30–40°	60–70°	80–90°
0	0.043	0.072 ± 0.002	0.072 ± 0.002	0.073 ± 0.002	0.073 ± 0.002
1	0.115	0.132 ± 0.002	0.133 ± 0.002	0.134 ± 0.002	0.128 ± 0.002
2	0.170	0.172 ± 0.002	0.173 ± 0.002	0.172 ± 0.002	0.164 ± 0.002
3	0.182	0.177 ± 0.004	0.176 ± 0.004	0.175 ± 0.004	0.176 ± 0.005
4	0.159	0.169 ± 0.005	0.170 ± 0.005	0.170 ± 0.005	0.184 ± 0.007
5	0.121	0.112 ± 0.003	0.113 ± 0.003	0.114 ± 0.003	0.118 ± 0.005
6	0.082	0.041 ± 0.003	0.040 ± 0.003	0.038 ± 0.004	0.035 ± 0.006

Note. Typical reduced χ^2 values ranged from ~2 to 15.

Table 2
Temperature Derived With Different Sets of Fixed Vibrational Population for 14–16 May 2019 Disk Spectra

	Temperature (K)		
SZA bin	Fixed v' at 80–90° SZA	Fixed v' at 0–10° SZA	(2,0) Band with fixed FCF
0–10°	587 ± 9	583 ± 9	621 ± 8
30–40°	594 ± 9	590 ± 9	623 ± 8
60–70°	654 ± 10	651 ± 10	677 ± 10
80–90°	752 ± 15	750 ± 15	777 ± 6

Note. Notice that temperature derived using (2,0) band and theoretical FCF is different from others.

the atmospheric pressure is higher compared to 200–250 km. Otherwise, the relative vibrational populations do not differ significantly, but, they are all different from the theoretical FCF populations. The lower vibrational levels ($v' < 2$) for all altitude bins are significantly enhanced relative to the theoretical FCF (by a factor of ∼1.93 at 100–150 km for $v' = 0$) as previous studies have reported (e.g., Ajello et al., 2020; Budzien et al., 1994). Similar to the SZA binned case, the $v' = 4$, and additionally the $v' = 3$ populations have more scatter and higher uncertainties. These most likely occurs because the $v' = 4$ and the $v' = 3$ bands that overlap with the atomic lines at 141.2 and 149.3 nm, respectively are removed from fitting. The $v' = 6$ relative populations are significantly (>50%) lower than the relative FCF populations due to pre-dissociation.

Analyses were also performed for different longitudes (eastern and western limb) and seasons (November and May). Relative vibrational populations for eastern (6–10 UT) and western (18–22 UT) limb for the 100–150 km and 200–250 km tangent altitude bins are shown in Table 3. These populations are also almost identical and no longitudinal variation is observed. Eastern limb's (6–10 UT) vibrational populations at 100–150 and 200–250 km bins on 14–16 May 2019 and 15–30 November 2018 are shown in Table 4. These populations also do not differ significantly and no seasonal dependence is seen.

The enhancement of $v' = 0$ at 100–150 and 150–200 km compared to 200–250 km (lower pressure) suggests potential pressure dependence (see Tables 3 and 4). However, below ∼150 km, O_2 photoabsorption in the Schumann-Runge (S-R) continuum attenuates the LBH bands. While the attenuation is especially significant below 100 km, it could affect the relative vibrational populations at 100–150 km. We used the Naval Research Lab Mass Spectrometer Incoherent Scatter Radar-00 (NRLMSIS-00, Picone et al., 2002) O_2 density profile and the O_2 photoabsorption cross section (from Gibson et al., 1983) to calculate the photoabsorption optical depth from 100 to 150 km at 1 km increments. Their average is assumed to be the "effective" optical depth for 100–150 km. Using the "effective" optical depth to attenuate the 200–250 km spectra (expected to have negligible photoabsorption), we found that the relative change in the band peaks (compared to 200–250 km spectra) are mostly within the spectral uncertainties. Only the LBH band peak near 155.5 nm with the only contribution from $v' = 0$ (see Figure 6) is slightly higher than the 1-σ uncertainty. But, our calculation of the optical depth did not account for the LBH contribution function (Figure 2). The spectra from altitudes near 150 km will contribute more to the signal, and for these altitudes, the calculated optical depths were only slightly smaller than 1. Additionally, a recent study using GOLD's stellar occultation observations showed that the NRLMSIS-00 O_2 densities were ∼10%–30% greater than measurements around 100–240 km (Lumpe et al., 2020). Therefore, the O_2 photoabsorption optical depth we calculated is most likely an overestimate of actual optical depth. Thus, the effect of O_2 photoabsorption on the relative LBH vibrational populations at 100–150 km are assumed to be negligible.

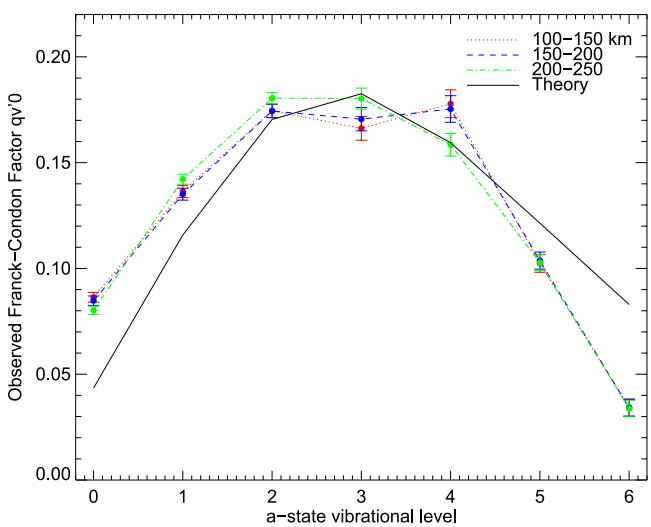

Figure 7. The relative vibrational populations using the Levenberg-Marquardt (LM) fit at 100–150 km (red and dotted), 150–200 km (blue and dashed) and 200–250 km (green and dash dotted) tangent altitudes during 14–16 May 2019 at 6–10 UT (shown in Figure 3). Theoretical FCF vibrational populations are shown in black for reference.

The uncertainties (obtained from the minimized LM fit's co-variance matrix) in vibrational populations for both SZA and tangent altitude bins are ∼10%. To verify these uncertainties, we used the monte-carlo method on the 14–16 May 2019 disk spectra at 30–40° SZA. We varied the spectra randomly up to ± measurement uncertainty 1,000 times and derived the vibrational populations. The standard deviations of the vibrational populations were consistent with the uncertainties obtained from LM fit's co-variance matrix (see chapter 8 in Bevington et al., 1993). The fitted minimum χ^2 ranged from ∼2 to 20. Higher χ^2 values most likely results from using a constant wavelength shift (optimized to match the band peak near 138 nm) and Gaussian FWHM for a given fit. GOLD's release note shows that the wavelength shifts and Gaussian FWHMs change at different slit locations and wavelength (Figures 3–10 and 3–11, respectively, in the release note). We attempted to limit this effect by using two different shift parameters (one for below and the other for

Table 3
The Relative Vibrational Populations at 100–150 and 200–250 km Tangent Altitude Bins on 14–16 May 2019 for Eastern (6–10 UT) and Western (18–22 UT) Limbs

		100–150 km		200–250 km	
v′ level	FCF	East	West	East	West
0	0.043	0.086 ± 0.002	0.083 ± 0.002	0.080 ± 0.002	0.081 ± 0.002
1	0.115	0.137 ± 0.003	0.132 ± 0.002	0.143 ± 0.002	0.144 ± 0.002
2	0.170	0.174 ± 0.003	0.172 ± 0.003	0.181 ± 0.003	0.180 ± 0.002
3	0.182	0.167 ± 0.006	0.170 ± 0.005	0.181 ± 0.005	0.179 ± 0.004
4	0.159	0.177 ± 0.006	0.179 ± 0.006	0.158 ± 0.005	0.157 ± 0.005
5	0.121	0.102 ± 0.004	0.106 ± 0.004	0.102 ± 0.004	0.105 ± 0.003
6	0.082	0.033 ± 0.004	0.035 ± 0.004	0.033 ± 0.004	0.032 ± 0.003

Note. Typical reduced χ^2 values ranged from ∼5 to 20.

above 146 nm), but this step still resulted in data-model band peak location mismatch at other places and similarly higher χ^2 values. We limit the effect of significantly different FWHM and wavelength shifts by only summing data around fixed slit locations where the variations are smaller. Other minor factors for higher χ^2 values could be co-adding spectra from different thermospheric temperatures, and decrease in detector sensitivity at wavelengths >150 nm, etc. Additionally, there are weak features that are present in GOLD's atmospheric spectra (e.g., near 148 and 155 nm), but not in the model or the lab spectra (Figure 7 in McClintock, Eastes, Hoskins et al., 2020). We removed these unknown features from the fit and it resulted in minor decrease in the χ^2 values. Since most of the optimized χ^2 values are >1 in the manuscript, we scale the derived parameter's uncertainties as suggested in Bevington et al. (1993, Chapter 8).

4.3. Comparison Between the Disk and Limb Vibrational Populations

The effective LBH emission altitude for disk observation is ∼150 km for SZA < 70 (see Figure 2). Thus, we use the 14–16 May 2019 Western limb spectra averaged from 140 to 160 km to compare with the disk vibrational populations from the same day. We binned the limb spectra (140–150 km) at 0–10°, 30–40° and 60–70° SZA and performed the spectral fitting. Figure 8 shows that the populations are consistent with both the regular disk and limb populations for the same day.

5. Summary

We have quantified relative LBH band vibrational populations as a function of SZA and tangent altitudes corresponding to GOLD's disk and limb dayglow measurements. Binning by tangent altitude and SZA is

Table 4
The Relative Vibrational Populations at 100–150 and 200–250 km Tangent Altitude Bins on 14–16 May 2019 and 15–30 November 2018 for Eastern Limb (6–10 UT)

		100–150 Km		200–250 Km	
v′ level	FCF	May	November	May	November
0	0.043	0.086 ± 0.002	0.082 ± 0.002	0.080 ± 0.002	0.078 ± 0.002
1	0.115	0.137 ± 0.003	0.137 ± 0.003	0.143 ± 0.002	0.143 ± 0.003
2	0.170	0.174 ± 0.003	0.173 ± 0.003	0.181 ± 0.003	0.180 ± 0.003
3	0.182	0.167 ± 0.006	0.172 ± 0.005	0.181 ± 0.005	0.187 ± 0.005
4	0.159	0.177 ± 0.006	0.172 ± 0.006	0.158 ± 0.005	0.151 ± 0.006
5	0.121	0.102 ± 0.004	0.106 ± 0.004	0.102 ± 0.004	0.103 ± 0.004
6	0.082	0.033 ± 0.004	0.036 ± 0.004	0.033 ± 0.004	0.035 ± 0.005

Note. Typical reduced χ^2 values ranged from ∼5 to 20.

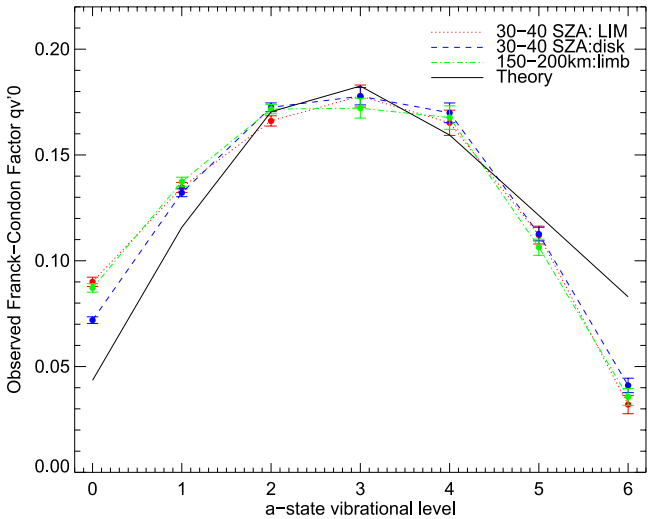

Figure 8. The relative vibrational populations for limb observations (14–16 May 2019) at 140–150 km and further binned at 30–40° solar zenith angle (SZA) is shown in red (and dotted). The disk vibrational populations binned at 30–40° SZA is shown in blue (and dashed) and the regular limb vibrational population at 150–200 km tangent altitude is shown in green (and dash dotted) for the same time period. Theoretical vibrational populations are shown in black for reference.

equivalent to binning by atmospheric pressure. For all SZAs and tangent altitudes, lower v' populations are enhanced compared to their theoretical FCF values. This suggests that, for thermospheric LBH dayglow emission, cascade processes are significant. Energy threshold effects can have a minor contribution to the low v' enhancement in dayglow emissions. Similar low v′ enhancement was also reported previously in studies that quantified thermospheric LBH dayglow population using limb measurements (see e.g., Budzien et al., 1994). All the $v' = 6$ vibrational populations are significantly (>50%) lower than the FCF populations due to pre-dissociation. The derived set of relative vibrational populations for different SZA and tangent altitude bins are quite similar to each other. Only the $v' = 0$ vibrational populations are enhanced significantly (factor of 1.93 with respect to FCF at 100–150 km) at 100–150 and 150–200 km where the pressure is higher (and O_2 photoabsorption more significant) compared to 200–250 km. The $v' = 0$ level is enhanced by a factor of ∼1.8 at 200–250 km with respect to FCF. Vibrational populations for $v' > 0$ at different tangent altitude bins did not change significantly with respect to each other. Thermospheric temperature retrievals using LBH spectra need these vibrational populations as fixed or varying parameters. Using any set of vibrational populations obtained here for different SZA bins does not change the retrieved disk temperatures significantly (<5 K). Thus, same set of vibrational populations can used in temperature retrievals reducing the uncertainties and run-times.

Data Availability Statement

GOLD L1C limb and disk spectra used for this study can be accessed at the GOLD Science Data Center (http://gold.cs.ucf.edu/search/) and at NASA's Space Physics Data Facility (https://spdf.gsfc.nasa.gov).

Acknowledgments
This work has been supported by NSF grants AGS 1853618 and 2031349 and NASA contract 80GSFC18C0061 to the University of Colorado, Boulder. We would also like to thank John Correira at Computational Physics, Inc. for valuable inputs to the LBH band model.

References

Ajello, J. M. (1970). Emission cross sections of N_2 in the vacuum ultraviolet by electron impact. *The Journal of Chemical Physics*, *53*(3), 1156–1165. https://doi.org/10.1063/1.1674113

Ajello, J. M., Evans, J. S., Veibell, V., Malone, C. P., Holsclaw, G. M., Hoskins, A. C., et al. (2020). The UV spectrum of the Lyman-Birge-Hopfield band system of N_2 induced by cascading from electron impact. *Journal of Geophysical Research: Space Physics*, *125*(3), e2019JA027546. https://doi.org/10.1029/2019ja027546

Ajello, J. M., Malone, C., Holsclaw, G., Hoskins, A., Eastes, R., McClintock, W., & Johnson, P. (2017). Electron impact study of the 100 ev emission cross section and lifetime of the Lyman-Birge-Hopfield band system of N_2: Direct excitation and cascade. *Journal of Geophysical Research: Space Physics*, *122*(6), 6776–6790. https://doi.org/10.1002/2017ja024087

Ajello, J. M., Mangina, R., & Meier, R. (2010). UV molecular spectroscopy from electron impact for applications to planetary atmospheres and astrophysics. *Charged Particle and Photon Interactions With Matter: Recent Advances, Applications, and Interfaces*, 761–804.

Ajello, J. M., & Shemansky, D. (1985). A reexamination of important N_2 cross sections by electron impact with application to the dayglow: The Lyman-Birge-Hopfield band system and N I (119.99 nm). *Journal of Geophysical Research*, *90*(A10), 9845–9861. https://doi.org/10.1029/ja090ia10p09845

Aksnes, A., Eastes, R., Budzien, S., & Dymond, K. (2006). Neutral temperatures in the lower thermosphere from N_2 Lyman-Birge-Hopfield (LBH) band profiles. *Geophysical Research Letters*, *33*(15), L15103. https://doi.org/10.1029/2006gl026255

Aryal, S., Evans, J., Correira, J., Burns, A. G., Wang, W., Solomon, S. C., et al. (2020). First global-scale synoptic imaging of solar eclipse effects in the thermosphere. *Journal of Geophysical Research: Space Physics*, *125*(9), e2020JA027789. https://doi.org/10.1029/2020ja027789

Benesch, W., Vanderslice, J. T., Tilford, S., & Wilkinson, P. (1966). Franck-condon factors for permitted transitions in N_2. *The Astrophysical Journal*, *144*, 408. https://doi.org/10.1086/148614

Bevington, P. R., Robinson, D. K., Blair, J. M., Mallinckrodt, A. J., & McKay, S. (1993). Data reduction and error analysis for the physical sciences. *Computers in Physics*, *7*(4), 415–416. https://doi.org/10.1063/1.4823194

Budzien, S., Feldman, P., & Conway, R. (1994). Observations of the far ultraviolet airglow by the ultraviolet limb imaging experiment on STS-39. *Journal of Geophysical Research*, *99*(A12), 23275–23287. https://doi.org/10.1029/94ja01543

Cartwright, D. C. (1978). Vibrational populations of the excited states of N2 under auroral conditions. *Journal of Geophysical Research*, *83*(A2), 517–531. https://doi.org/10.1029/ja083ia02p00517

Cartwright, D. C., Chutjian, A., Trajmar, S., & Williams, W. (1977a). Electron impact excitation of the electronic states of N 2. I. Differential cross sections at incident energies from 10 to 50 ev. *Physics Review A*, *16*(3), 1013–1040. https://doi.org/10.1103/PhysRevA.16.1013

Cartwright, D. C., Trajmar, S., Chutjian, A., & Williams, W. (1977b). Electron impact excitation of the electronic states of N_2. II. Integral cross sect$_i$ons at incident energies from 10 to 50 ev. *Physics Review A*, *16*, 1041–1051. https://doi.org/10.1103/PhysRevA.16.1041

Eastes, R. (2000). Modeling the N_2 Lyman-Birge-Hopfield bands in the dayglow: Including radiative and collisional cascading between the singlet states. *Journal of Geophysical Research*, *105*(A8), 18557–18573. https://doi.org/10.1029/1999ja000378

Eastes, R., & Dentamaro, A. (1996). Collision-induced transitions between the a1Πg, a′1Σu−, and W1Δu states of N_2: Can they affect auroral N2 Lyman-Birge-Hopfield band emissions? *Journal of Geophysical Research*, *101*(A12), 26931–26940. https://doi.org/10.1029/96ja01636

Eastes, R., Feldman, P., Gentieu, E., & Christensen, A. (1985). The ultraviolet dayglow at solar maximum: 1. Far UV spectroscopy at 3.5 Å resolution. *Journal of Geophysical Research*, *90*(A7), 6594–6600. https://doi.org/10.1029/ja090ia07p06594

Eastes, R., McClintock, W., Burns, A., Anderson, D., Andersson, L., Codrescu, M., et al. (2017). The global-scale observations of the limb and disk (gold) mission. *Space Science Reviews*, *212*(1–2), 383–408. https://doi.org/10.1007/s11214-017-0392-2

Evans, J., Lumpe, J., Correira, J., Veibell, V., Kyrwonos, A., McClintock, W., et al. (2020). Neutral exospheric temperatures from the gold mission. *Journal of Geophysical Research: Space Physics*, *125*(9), e2020JA027814. https://doi.org/10.1029/2020ja027814

Gibson, S., Gies, H., Blake, A., McCoy, D., & Rogers, P. (1983). Temperature dependence in the Schumann-Runge photoabsorption continuum of oxygen. *Journal of Quantitative Spectroscopy and Radiative Transfer*, *30*(5), 385–393. https://doi.org/10.1016/0022-4073(83)90101-2

Laskar, F., Eastes, R., Codrescu, M., Evans, J., Burns, A., Wang, W., et al. (2021). Response of gold retrieved thermospheric temperatures to geomagnetic activities of varying magnitudes. *Geophysical Research Letters*, *48*(15), e2021GL093905. https://doi.org/10.1029/2021gl093905

Lean, J., Warren, H., Mariska, J., & Bishop, J. (2003). A new model of solar EUV irradiance variability 2. Comparisons with empirical models and observations and implications for space weather. *Journal of Geophysical Research*, *108*(A2), 1059. https://doi.org/10.1029/2001ja009238

Levenberg, K. (1944). A method for the solution of certain non-linear problems in least squares. *Quarterly of Applied Mathematics*, *2*(2), 164–168. https://doi.org/10.1090/qam/10666

Lofthus, A., & Krupenie, P. H. (1977). The spectrum of molecular nitrogen. *Journal of Physical and Chemical Reference Data*, *6*(1), 113–307. https://doi.org/10.1063/1.555546

Lumpe, J., McClintock, W., Evans, J., Correira, J., Veibell, V., Beland, S., & Eastes, R. (2020). A new data set of thermospheric molecular oxygen from the global-scale observations of the limb and disk (gold) mission. *Journal of Geophysical Research: Space Physics*, *125*(4), e2020JA027812. https://doi.org/10.1029/2020ja027812

Marquardt, D. W. (1963). An algorithm for least-squares estimation of nonlinear parameters. *Journal of the Society for Industrial and Applied Mathematics*, *11*(2), 431–441. https://doi.org/10.1137/0111030

McClintock, W. E., Eastes, R. W., Beland, S., Bryant, K. B., Burns, A. G., Correira, J., et al. (2020a). Global-scale observations of the limb and disk mission implementation: 2. Observations, data pipeline, and level 1 data products. *Journal of Geophysical Research: Space Physics*, *125*(5), e2020JA027809. https://doi.org/10.1029/2020ja027809

McClintock, W. E., Eastes, R. W., Hoskins, A. C., Siegmund, O. H., McPhate, J. B., Krywonos, A., et al. (2020b). Global-scale observations of the limb and disk mission implementation: 1. Instrument design and early flight performance. *Journal of Geophysical Research: Space Physics*, *125*(5), e2020JA027797. https://doi.org/10.1029/2020ja027797

Meier, R., Picone, J., Drob, D., Bishop, J., Emmert, J., Lean, J., et al. (2015). Remote sensing of earth's limb by TIMED/GUVI: Retrieval of thermospheric composition and temperature. *Earth and Space Science*, *2*(1), 1–37. https://doi.org/10.1002/2014ea000035

Paxton, L. J., Christensen, A. B., Humm, D. C., Ogorzalek, B. S., Pardoe, C. T., Morrison, D., et al. (1999). Global ultraviolet imager (GUVI): Measuring composition and energy inputs for the NASA thermosphere ionosphere mesosphere energetics and dynamics (timed) mission. *Optical spectroscopic techniques and instrumentation for atmospheric and space research III*, *3756*, 265–276.

Picone, J., Hedin, A., Drob, D. P., & Aikin, A. (2002). Nrlmsise-00 empirical model of the atmosphere: Statistical comparisons and scientific issues. *Journal of Geophysical Research*, *107*(A12). 1468. https://doi.org/10.1029/2002ja009430

Strickland, D., Meier, R., Walterscheid, R., Craven, J., Christensen, A., Paxton, L., et al. (2004). Quiet-time seasonal behavior of the thermosphere seen in the far ultraviolet dayglow. *Journal of Geophysical Research*, *109*(A1), A01302. https://doi.org/10.1029/2003ja010220

Young, J., Malone, C., Johnson, P., Ajello, J., Liu, X., & Kanik, I. (2010). Lyman–Birge–Hopfield emissions from electron-impact excited N_2. *Journal of Physics B: Atomic, Molecular and Optical Physics*, *43*(13), 135201. https://doi.org/10.1088/0953-4075/43/13/135201

Erratum

Goddard Space Flight Center grant information has been added to the Acknowledgments section. This version may be considered the authoritative version of record.